Journal of Colloid and Interface Science 526 (2018) 322–336

Contents lists available at ScienceDirect

Journal of Colloid and Interface Science

journal homepage: www.elsevier.com/locate/jcis

Regular Article

Controlled hydrothermal synthesis of bismuth oxychloride/bismuth oxybromide/bismuth oxyiodide composites exhibiting visible-light photocatalytic degradation of 2-hydroxybenzoic acid and crystal violet

Ciao-Wei Siao [a], Hung-Lin Chen [b], Li-Wen Chen [a], Jia-Lin Chang [a], Tsung-Wen Yeh [a], Chiing-Chang Chen [a,*]

[a] Department of Science Education and Application, National Taichung University of Education, 403, Taiwan
[b] Department of Chemistry, National Central University, Taoyuan 320, Taiwan

GRAPHICAL ABSTRACT

Figure abstract. Schematic diagram of synthesis method and photcatalysis for as-prepared $BiO_xCl_y/BiO_mBr_n/BiO_pI_q$ under different conditions.

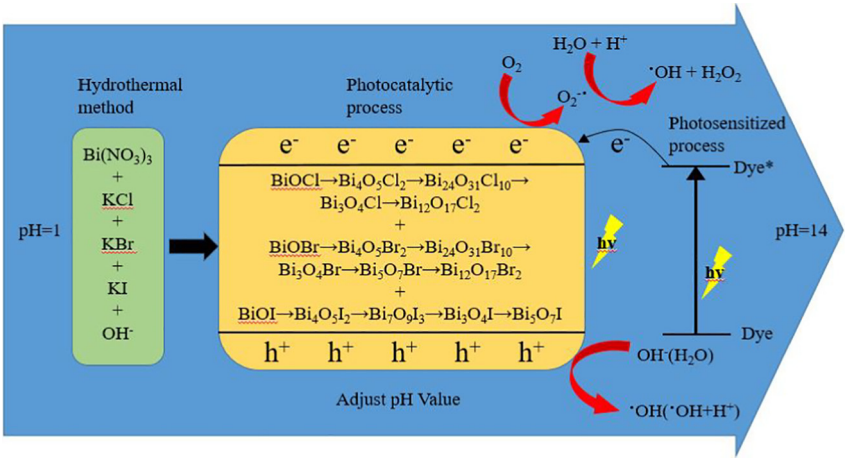

ARTICLE INFO

Article history:
Received 25 January 2018
Revised 23 April 2018
Accepted 25 April 2018
Available online 26 April 2018

Keywords:
Photocatalysis
$BiO_xCl_y/BiO_mBr_n/BiO_pI_q$
Composites
2-Hydroxybenzoic acid
Crystal violet

ABSTRACT

This paper presents an unprecedented systematic synthetic study of a controlled hydrothermal method for the preparation of bismuth oxychloride/bismuth oxybromide/bismuth oxyiodide ternary composites ($BiO_xCl_y/BiO_mBr_n/BiO_pI_q$). The pH, temperature, and KCl:KBr:KI molar ratio for the reactions were adjusted to control the compositions and morphologies of $BiO_xCl_y/BiO_mBr_n/BiO_pI_q$ composites. Scanning electron microscopy-energy dispersive X-ray spectroscopy, transmission electron microscopy, X-ray diffraction, ultraviolet–visible diffuse reflectance spectroscopy, Brunauer–Emmett–Teller specific surface areas, photoluminescence spectroscopy, and X-ray photoelectron spectroscopy, and electron paramagnetic resonance spectroscopy were applied to the products. The photocatalytic activities of dispersions were examined by monitoring the 2-hydroxybenzoic acid (HBA) and crystal violet concentrations. Various scavengers demonstrated quenching effects. $O_2^{\bullet-}$ was crucial to HBA degradation, whereas h^+ and ·OH played minor roles in HBA degradation. This text hypothesizes possible photodegradation mechanisms.

* Corresponding author.
E-mail address: ccchen@mail.ntcu.edu.tw (C.-C. Chen).

https://doi.org/10.1016/j.jcis.2018.04.097
0021-9797/

1. Introduction

The need to remove toxins from wastewater has become impossible to ignore over the past two decades. Toxic pollutants pose grave dangers to the environment and living beings. The ecological survival processes of numerous plants involve 2-salicylic or 2-hydroxybenzoic acid (HBA), a plant hormone that is used worldwide in aspirin and in various food, cosmetic, pharmaceutical, and dermatological products and can harm the environment. HBA has been detected in 50 ppm concentrations in urban wastewater, rivers, and wastewater [1,2]. Wastewater treatment does not usually eliminate HBA. Even before aspirin was commoditized as an analgesic and anti-inflammatory product, physicians used plants that were rich in mono-HBAs and their metabolic precursors to prevent and cure various chronic diseases. Pharmacologists have studied HBA, recognizing that aspirin, in addition to other products derived from HBA, can be administered to prevent and remedy myriads of metabolic disorders [3]. HBA is a bioactive constituent of several traditional medicines [4]. Numerous plants that contain HBA are adaptogenic; in other words, these plants seem to improve stress resistance [5]. Several studies have addressed HBA decomposition using photocatalysts in active-species-generating systems that include ZnO [6], Al/Fe_2O_3 [7], TiO_2/MWCNT [8], and La_2O_3/TiO_2 [9].

Around million tons and more than ten thousand different synthetic dyes and pigments are generated annually worldwide, and these are used extensively in the dye and printing industries. It is evaluated that about ten percent are lost in industrial effluents. Dyestuffs from the textile and photographic industries are becoming a major source of environmental pollution. Triarylmethane (TAM) dyes are suitable for a large variety of technological applications. The paper, leather, cosmetic, and food industries make use of TAM dyes as agents for the coloring of fats, plastics, oils, varnishes, and waxes and are major consumers for various types of TAM dyes. TAM dyes are also used as staining agents in bacteriological and histopathological applications as well. TAM dyes have potential for application to photodynamic treatments, but intensive research has proven that reactive oxygen species cause TAM to be photocytotoxic [10]. Thyroid peroxidase-catalyzed TAM dye oxidation in living organisms is dangerous, in that the mentioned process yields diverse *N*-de-alkylated aromatic amines exhibiting similar structures to carcinogenic aromatic amines [11]. Scholars have proven the appropriateness of applying TAM dyes as targetable senitizers in photodecomposing specific cells (or cellular components) [10,11].

Researchers have applied photocatalysts to degrade TAM dye pollutants in wastewater [12]. Several active-specifies generating systems have been applied for studying crystal violet (CV) dye decomposition, some of which include TiO_2 [13], Bi_2WO_6 [14], CuS/Bi_2S_3 [15], Ag/$AgVO_3$ [16], $Bi_xAg_yO_z$ [17], BiOI/g-C_3N_4 [18], Bi_2SiO_5/g-C_3N_4 [19], and $SrFeO_{3-x}$/g-C_3N_4 [20]; in the majority of scenarios, scholars have adequately confirmed the correspoding reaction kinetics, mechanics, and activities. Visible-light-driven photocatalysts hold promise as pollution treatments. Bismuth oxyhalides [15,21], which have been proven to possess remarkable photocatalytic efficiency, are multicomponent metal oxyhalides that belong to the V–VI–VII family. Their photocatalytic activity arises from static electrical forces perpendicular to their layered structures, which separate photoformed electron–hole pairs.

Researchers have theorized that a photocatalyst's morphology, size, and properties must be closely related; therefore, researchers have expected photocatalysts with hierarchical architectures to exhibit high efficiency. To improve a photocatalyst's activity, one can combine composites; it is highly probable that such combinations may favorably modify electronic properties and efficiently separate photoformed electron–hole pairs [12]. Keller et al. [22] first researched the BiOX/BiOY (X, Y = Cl, Br, or I) system's solubility and found it to be nearly unlimited. Subsequent studies have oxyhalide materials similar to the aforementioend ones have been synthesized, with the materials exhibiting unique photocatalytic properties. For example, by using series binary BiOX/BiOY (X, Y = Cl, Br, or I), Chen et al. [20-24] have prepared a system for CV removal that is galvanized by visible light and is highly efficient, which is due to the BiOX/BiOY photoinduced charge carriers being separated and transfered effectively, thus engendering a narrower bandgap and a more negative position for the conduction band and consequently favoring the photogenerated holes. To promote the degradation task of bisphenol-A, Zhang et al. [25] irradiated BiOCl/BiOI phases with visible light and produced high photocatalytic activities. Dong et al. [26] coprecipitated BiOCl/BiOI and observed that under irradiation provided by visible light, the speed of NO removal observed for their material was greater than that observed for TiO_2 by four times. Furthermore, results derived from diffuse reflectance spectroscopy (DRS) analysis and large photocurrent observations demonstrated BiOI/BiOCl to absorb visible light, thus conducing electron–hole pair development and segregation [26].

In the current study, a series of ternary $BiO_xCl_y/BiO_mBr_n/BiO_pI_q$ photocatalysts were synthesized and characterized, thus constituting the first systematic synthetic study conducted on $BiO_xCl_y/BiO_mBr_n/BiO_pI_q$ based on controlled hydrothermal synthesis. The efficiencies of $BiO_xCl_y/BiO_mBr_n/BiO_pI_q$ photocatalysts under irradiation provided by visible light were evaluated; the evaluation entailed the measurement of HBA and CV degradation rates. Under irradiation provided by visible light, the aqueous HBA and CV removal rates observed for these ternary composites were considerably faster than those observed for unitary bismuth oxyhalides. Both quenchers and electron paramagnetic resonance (EPR) spectroscopy were applied to elucidate the HBA and CV degradation mechanism by measuring the photocatalysis of active species.

2. Experiment

2.1. Materials

The entirety of the applied chemicals in this study were of analytic grade, with no subjection to additional purification. The following, in addition, were purchased: HBA (2-hydroxybenzoic acid or salicylic acid), $Bi(NO_3)_3{\cdot}5H_2O$, KI, KBr (Katayama), KCl (Shimakyu), CV dye (TCI), sodium azide (Sigma), *p*-benzoquinone (Alfa Aesar), isopropanol (Merck), and ammonium oxalate (Osaka). Furthermore, reagent-grade ammonium acetate, sodium hydroxide, nitric acid, and HPLC-grade methanol were obtained from Merck.

2.2. Instruments and analytical methods

Scanning electron microscopy-energy dispersive spectroscopy (SEM-EDS) was measured using a JEOL JSM-7401F microscope, with the acceleration voltage being set to 15 kV. Moreover, a JEOL-2010 microscope was applied for the measurement of transmission electron microscopy (TEM) images, EDS spectra, high-resolution TEM images, and selected-area electron diffraction patterns, with the acceleration voltage being set at 200 kV. High-resolution X-ray photoelectron spectroscopy (XPS) was recorded with an ULVAC-PHI spectrometer. Al-Kα radiation was also realized at 15 kV; a Scinco SA-13.1 spectrophotometer recorded ultraviolet–visible (UV–Vis) DRS data within the 300–800 nm wavelength range at room temperature. A diffractometer system (MAC Science MXP18) applying Cu-Kα radiation (40 kV and 80 mA) recorded X-ray diffraction (XRD) patterns. UV photoelectron spectroscopy data were

measured with an ULVAC-PHI XPS PHI Quantera SXM, and photoluminescence (PL) data were measured with a Hitachi F-7000. An automated system (Micromeritics Gemini) recorded the samples' Brunauer–Emmett–Teller (BET) specific surface areas (S_{BET}) at 237 °C; in this process, nitrogen gas was utilized as the adsorbate at liquid-nitrogen temperature. Finally, a Brüker ER200D spectrometer, with an Agilent 5310A frequency counter operating in the X band, recorded EPR spectra at 77 K.

2.3. Synthesis of a $BiO_xCl_y/BiO_mBr_n/BiO_pI_q$ series

A flask possessing 50-mL capacity was filled with 5 mmol Bi $(NO_3)_3{\cdot}5H_2O$, after which 4 M nitric acid (5 mL) was added. The contents of the flask were continuously stirred, with the addition of 2 M sodium hydroxide dropwise for achieving pH value adjustment. After the observation of precipitate formation, 3 M portions of KCl, KBr, and KI (with various KCl: KBr: KI molar ratios) were added dropwise. The solution underwent 30 min of vigorous stirring, followed by transferring it to a 30-mL Teflon-lined stainless steel autoclave; next, the autoclave was exposed to heating temperatures ranging from 100 to 250 °C for 12 h, and it was subsequently allowed to cool to room temperature. After these processes, the solid obtained was subjected to filtration, washing performed using deionized water and ethanol for ionic species removal, and then overnight drying at 80 °C. A selection of $BiO_xCl_y/BiO_mI_n/BiO_pI_q$ composites were prepared with controlled values of KCl:KBr:KI molar ratio (1:1:1; 3:1:1; 1:3:1; or 1:1:3), temperature, pH, and reaction times, as indicated in Table 1. The as-synthesized samples were labeled with identifiers that ranged from BC1B1I1-1-100-12 to BC1B1I3-250-12.

2.4. Photocatalytic experiments

In the trials of this study, we chose either HBA (or CV) as our target pollutant to evaluate photocatalytic activity. HBA (or CV) irradiation products were immersed in stirred aqueous solutions housed in flasks (100 mL); both an aqueous dispersion of 10 ppm 100 mL HBA (or CV) and 10 mg of the photocatalyst were then placed in a Pyrex flask. The suspension's pH was adjusted through sodium hydroxide or nitric acid solution addition. After batch sorption experiments had been conducted, the mixture underwent a centrifugation procedure conducted at 3000 rpm to determine the absorbance of HBA (or CV) at 298 (or 588) nm through UV-PDA. Irradiation was supplied by 10-W Xe arc lamps at a fixed light intensity of 3.2 W/m^2, with a distance of 30 cm separating the reaction vessel and the light source. At specified irradiation time intermissions, 5-mL aliquots were collected and then underwent a centrifugation procedure for photocatalyst removal, and each supernatant sample was subsequently analyzed through UV-PDA.

3. Results and discussion

3.1. Characterization of $BiO_xCl_y/BiO_mBr_n/BiO_pI_q$ composites

3.1.1. Phase structure

Figs. 1 and **S1–S6** of Supplementary Materials illustrate the as-synthesized samples' XRD patterns, clearly indicating the coexistence of various phases. These samples were noted to contain BiOCl (JCPDS 85-0861), along with Bi_3O_4Cl (JCPDS 36-0760), $Bi_{12}O_{17}Cl_2$ (JCPDS 37-0702), BiOBr (JCPDS 09-0393), $Bi_4O_5Br_2$ (JCPDS 37-0669), Bi_3O_4Br (JCPDS 84-0793), Bi_5O_7Br (JCPDS 38-0493), BiOI (JCPDS 73-2062), $Bi_4O_5I_2$ [27], $Bi_7O_9I_3$ [28], Bi_5O_7I (JCPDS 40-0548), and α-Bi_2O_3 (JCPDS 41-1449). Notably, the XRD results derived after setting pH to 1, 4, 7, 10, 13, and 14 were the same as those obtained for the BiOCl and BiOBr primary phases, the BiOCl/BiOBr, BiOCl/BiOI, and BiOBr/BiOI binary phases, as well as the ternary phases including BiOCl/BiOBr/BiOI, BiOCl/$Bi_4O_5Br_2$/BiOI, Bi_3O_4Cl/BiOBr/BiOI, and $Bi_{12}O_{17}Cl_2$/Bi_3O_4Br/$Bi_4O_5I_2$; the quaternary phases including $Bi_{12}O_{17}Cl_2$/Bi_3O_4Br/$Bi_4O_5I_2$/Bi_5O_7I,

Table 1
Codes of $BiO_xCl_y/BiO_mBr_n/BiO_pI_q$ prepared under different KCl:KBr:KI molar ratio, pH values, and reaction temperatures at 12 h.

pH	Temperature (°C)			
	100	150	200	250
	Molar ratio = 1:1:1			
1	BC1B1I1-1-100-12	BC1B1I1-1-150-12	BC1B1I1-1-200-12	BC1B1I1-1-250-12
4	BC1B1I1-4-100-12	BC1B1I1-4-150-12	BC1B1I1-4-200-12	BC1B1I1-4-250-12
7	BC1B1I1-7-100-12	BC1B1I1-7-150-12	BC1B1I1-7-200-12	BC1B1I1-7-250-12
10	BC1B1I1-10-100-12	BC1B1I1-10-150-12	BC1B1I1-10-200-12	BC1B1I1-10-250-12
13	BC1B1I1-13-100-12	BC1B1I1-13-150-12	BC1B1I1-13-200-12	BC1B1I1-13-250-12
14	BC1B1I1-14-100-12	BC1B1I1-14-150-12	BC1B1I1-14-200-12	BC1B1I1-14-250-12
	Molar ratio = 3:1:1			
1	BC3B1I1-1-100-12	BC3B1I1-1-150-12	BC3B1I1-1-200-12	BC3B1I1-1-250-12
4	BC3B1I1-4-100-12	BC3B1I1-4-150-12	BC3B1I1-4-200-12	BC3B1I1-4-250-12
7	BC3B1I1-7-100-12	BC3B1I1-7-150-12	BC3B1I1-7-200-12	BC3B1I1-7-250-12
10	BC3B1I1-10-100-12	BC3B1I1-10-150-12	BC3B1I1-10-200-12	BC3B1I1-10-250-12
13	BC3B1I1-13-100-12	BC3B1I1-13-150-12	BC3B1I1-13-200-12	BC3B1I1-13-250-12
14	BC3B1I1-14-100-12	BC3B1I1-14-150-12	BC3B1I1-14-200-12	BC3B1I1-14-250-12
	Molar ratio = 1:3:1			
1	BC1B3I1-1-100-12	BC1B3I1-1-150-12	BC1B3I1-1-200-12	BC1B3I1-1-250-12
4	BC1B3I1-4-100-12	BC1B3I1-4-150-12	BC1B3I1-4-200-12	BC1B3I1-4-250-12
7	BC1B3I1-7-100-12	BC1B3I1-7-150-12	BC1B3I1-7-200-12	BC1B3I1-7-250-12
10	BC1B3I1-10-100-12	BC1B3I1-10-150-12	BC1B3I1-10-200-12	BC1B3I1-10-250-12
13	BC1B3I1-13-100-12	BC1B3I1-13-150-12	BC1B3I1-13-200-12	BC1B3I1-13-250-12
14	BC1B3I1-14-100-12	BC1B3I1-14-150-12	BC1B3I1-14-200-12	BC1B3I1-14-250-12
	Molar ratio = 1:1:3			
1	BC1B1I3-1-100-12	BC1B1I3-1-150-12	BC1B1I3-1-200-12	BC1B1I3-1-250-12
4	BC1B1I3-4-100-12	BC1B1I3-4-150-12	BC1B1I3-4-200-12	BC1B1I3-4-250-12
7	BC1B1I3-7-100-12	BC1B1I3-7-150-12	BC1B1I3-7-200-12	BC1B1I3-7-250-12
10	BC1B1I3-10-100-12	BC1B1I3-10-150-12	BC1B1I3-10-200-12	BC1B1I3-10-250-12
13	BC1B1I3-13-100-12	BC1B1I3-13-150-12	BC1B1I3-13-200-12	BC1B1I3-13-250-12
14	BC1B1I3-14-100-12	BC1B1I3-14-150-12	BC1B1I3-14-200-12	BC1B1I3-14-250-12

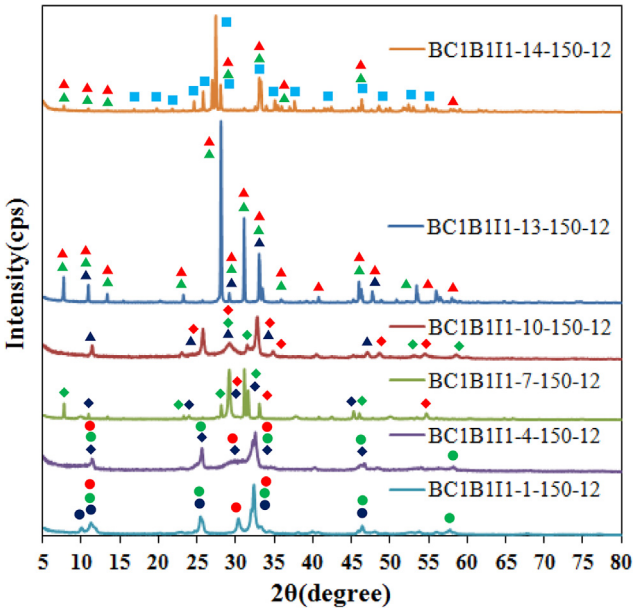

Fig. 1. XRD patterns of as-prepared $BiO_xCl_y/BiO_mBr_n/BiO_pI_q$ samples under different temperatures. (Molar ratio KCl:KBr:KI = 1:1:1, hydrothermal conditions: temp = 150 °C, pH = 1–14, time = 12 h).

$Bi_3O_4Cl/Bi_4O_5Br_2/BiOI/Bi_4O_5I_2$, and $Bi_3O_4Cl/Bi_3O_4Br/Bi_7O_9I_3/Bi_5O_7I$; and the quinary phases including $Bi_3O_4Cl/BiOBr/Bi_3O_4Br/BiOI/Bi_4O_5I_2$ and $Bi_{12}O_{17}Cl_2/Bi_3O_4Br/Bi_5O_7Br/Bi_7O_9I_3/Bi_5O_7I$. Table 2 summarizes the XRD measurements.

As Fig. 2 reveals, the $Bi_{12}O_{17}Cl_2/Bi_3O_4Br/Bi_4O_5I_2$ consisted of various sheets or plates of different sizes; this matched the observations obtained from the TEM process. The EDS spectrum revealed that the sample included elemental Bi, O, Cl, Br, and I. The samples' atomic ratios of Cl, Br, and I were within 0.63%, 4.40%, and 9.76%, respectively; these ratios corresponded to the sample. Moreover, as revealed by the HRTEM image, three lattice image sets were obtained, and the corresponding d-spacing values were 0.275, 0.286, and 0.199 nm; these were consistent with the XRD results and corresponded to the (1 1 9) plane of $Bi_{12}O_{17}Cl_2$, the (0 2 0) plane of Bi_3O_4Br, and the (0 2 0) plane of $Bi_4O_5I_2$ (Fig. 1), respectively. The results suggest that in the obtained composites, the $Bi_{12}O_{17}Cl_2/Bi_3O_4Br/Bi_4O_5I_2$ ternary phases had been established, which favored photoinduced carrier segregation, thus engndering high photocatalytic activity levels.

Furthermore, the results suggested that for the various applied pH values, the compounds manifested the following transformations: $BiOCl \rightarrow Bi_4O_5Cl_2 \rightarrow Bi_{24}O_{31}Cl_{10} \rightarrow Bi_3O_4Cl \rightarrow Bi_{12}O_{17}Cl_2 \rightarrow \alpha\text{-}Bi_2O_3$, $BiOBr \rightarrow Bi_4O_5Br_2 \rightarrow Bi_3O_4Br \rightarrow Bi_5O_7Br \rightarrow \alpha\text{-}Bi_2O_3$, and $BiOI \rightarrow Bi_4O_5I_2 \rightarrow Bi_7O_9I_3 \rightarrow Bi_3O_4I \rightarrow Bi_5O_7I \rightarrow \alpha\text{-}Bi_2O_3$. Some reactions that may have caused the formation of the $BiO_xCl_y/BiO_mBr_n/BiO_pI_q$ as-samples are formalized by Eqs. (1)–(26):

$$Bi^{3+}+3\ OH^- \rightarrow Bi(OH)_3\ (s) \quad (1)$$

$$Bi(OH)_3\ (s)+3Cl^- \rightarrow BiCl_3\ (s)+3\ OH^- \quad (2)$$

$$BiCl_3\ (s)+2\ OH^- \rightarrow BiOCl\ (s)+2Cl^-+H_2O \quad (3)$$

$$BiOCl\ (s)+2\ OH^- \rightarrow Bi_4O_5C_{l2}\ (s)+2Cl^-+H_2O \quad (4)$$

$$6Bi_4O_5Cl_2\ (s)+2\ OH^- \rightarrow Bi_{24}O_{31}Cl_{10}\ (s)+2Cl^-+H_2O \quad (5)$$

$$Bi_{24}O_{31}Cl_{10}\ (s)+2\ OH^- \rightarrow 8\ Bi_3O_4Cl\ (s)+2Cl^-+H_2O \quad (6)$$

$$5Bi_3O_4Cl\ (s)+2\ OH^- \rightarrow 3\ Bi_5O_7Cl\ (s)+2Cl^-+H_2O \quad (7)$$

$$12Bi_5O_7Cl\ (s)+2\ OH^- \rightarrow 5\ Bi_{12}O_{17}Cl_2\ (s)+2Cl^-+H_2O \quad (8)$$

$$Bi_{12}O_{17}Cl_2\ (s)+2\ OH^- \rightarrow 6\ Bi_2O_3\ (s)+2Cl^-+H_2O \quad (9)$$

$$2Bi(OH)_{3(s)}+Br^- \rightarrow BiOBr_{(s)}+H_2O+OH^- \quad (10)$$

$$Bi^{3+}+3Br^- \rightarrow BiBr_{3(s)} \quad (11)$$

$$BiBr_{3(s)}+2OH^- \rightarrow BiOBr_{(s)}+2Br^-+H_2O \quad (12)$$

$$4BiOBr_{(s)}+2OH^- \rightarrow Bi_4O_5Br_{2(s)}+2Br^-+H_2O \quad (13)$$

$$6Bi_4O_5Br_{2(s)}+2OH^- \rightarrow Bi_{24}O_{31}Br_{10(s)}+2Br^-+H_2O \quad (14)$$

$$Bi_{24}O_{31}Br_{10(s)}+2OH^- \rightarrow 8Bi_3O_4Br_{(s)}+2Br^-+H_2O \quad (15)$$

$$5Bi_3O_4Br_{(s)}+2OH^- \rightarrow 3Bi_5O_7Br_{(s)}+2Br^-+H_2O \quad (16)$$

$$12Bi_5O_7Br_{(s)}+2OH^- \rightarrow 5Bi_{12}O_{17}Br_{2(s)}+2Br^-+H_2O \quad (17)$$

$$Bi_{12}O_{17}Br_{2(s)}+2OH^- \rightarrow 6Bi_2O_{3(s)}+2Br^-+H_2O \quad (18)$$

$$2Bi(OH)_3\ (s)+I^- \rightarrow BiOI\ (s)+H_2O+OH^- \quad (19)$$

$$Bi^{3+}+3\ I^- \rightarrow BiI_3\ (s) \quad (20)$$

$$BiI_3\ (s)+2\ OH^- \rightarrow BiOI\ (s)+2\ I^-+H_2O \quad (21)$$

$$4BiOI\ (s)+2\ OH^- \rightarrow Bi_4O_5I_2\ (s)+2\ I^-+H_2O \quad (22)$$

$$7Bi_4O_5I_2\ (s)+2\ OH^- \rightarrow 4\ Bi_7O_9I_3\ (s)+2\ I^-+H_2O \quad (23)$$

$$3Bi_7O_9I_3\ (s)+2\ OH^- \rightarrow 7\ Bi_3O_4I\ (s)+2\ I^-+H_2O \quad (24)$$

$$5Bi_3O_4I\ (s)+2\ OH^- \rightarrow 3\ Bi_5O_7I\ (s)+2\ I^-+H_2O \quad (25)$$

$$2Bi_5O_7I\ (s)+2\ OH^- \rightarrow 5\ Bi_2O_3\ (s)+2\ I^-+H_2O \quad (26)$$

These equations indicate that at or near the beginning of the reaction, BiOCl (or BiOBr, BiOI) manifested, and that OH^- ions gradually were substituted for Cl^- (or Br^-, I^-) ions under the fundamental conditions; thus the products contained reduced amounts of Cl^- (or Br^-, I^-) ions. Ion chromatography (IC) was applied to confirm the Cl^- and I^- concentrations, according to their retention times [12]. As revealed by the IC results, with the progression of the hydrothermal procedure, the concentrations increased at the various applied pH values. The progress of the $BiO_xCl_y/BiO_mBr_n/BiO_pI_q$ hydrothermal synthesis can be tracked by monitoring the Cl^-, Br^-, and I^- ions formed in the solution using a tri-halo-semiconductor. These results suggested that OH^- ions displaced Cl^-, Br^-, and I^- ions slowly with the increase in the applied pH value, and thus the system produced $Bi_4O_5Cl_2$, $Bi_{24}O_{31}Cl_{10}$, Bi_3O_4Cl, Bi_5O_7Cl, $Bi_{12}O_{17}Cl_2$ (or BiOBr, $Bi_4O_5Br_2$, Bi_3O_4Br, Bi_5O_7Br, and $Bi_4O_5I_2$, $Bi_7O_9I_3$, Bi_3O_4I, Bi_5O_7I), and $\alpha\text{-}Bi_2O_3$; in short, high pH values were correlated with products that had low Cl^- (or Br^-, I^-) concentrations. In the final products, OH^- ions completely replaced the Cl^- (or Br^-, I^-) ions, and thus $\alpha\text{-}Bi_2O_3$ formed under strong basic conditions. The relationships between OH^-, Cl^-, Br^-, and I^- existing in aqueous solutions are typically competitive. In this study, a hydrothermal method was applied for selective preparation of $BiO_xCl_y/BiO_mBr_n/BiO_pI_q$ by control of the pH value, the molar ratio, and the reaction temperature.

Table 2
Crystalline phase changes of $BiO_xCl_y/BiO_mBr_n/BiO_pI_q$ nanosheets prepared under different reaction conditions.

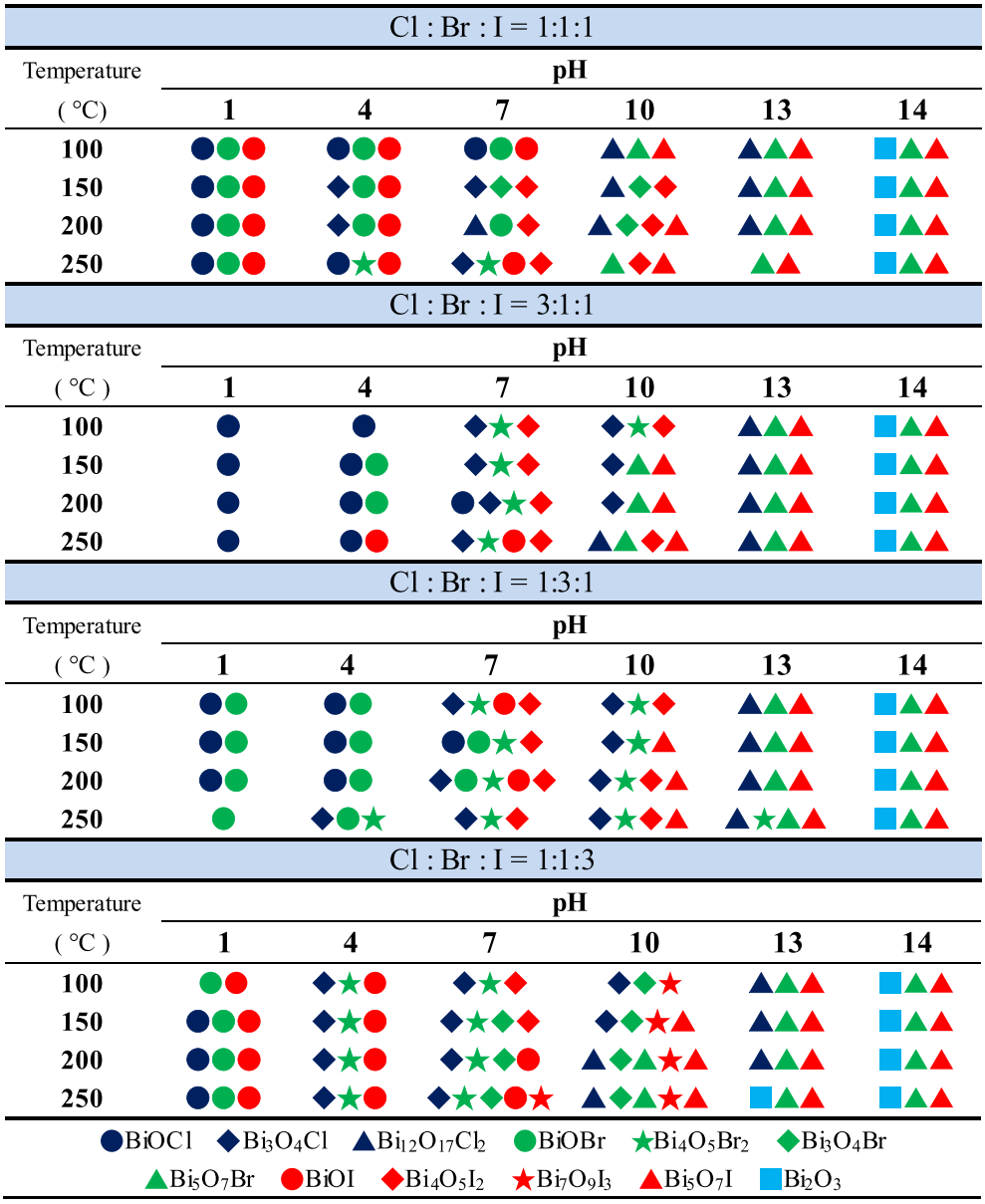

3.1.2. Morphological structure and composition

$BiO_xCl_y/BiO_mBr_n/BiO_pI_q$ was synthesized through the use of $Bi(NO_3)_3{\cdot}5H_2O$ and a combination of KCl, KBr, and KI (1:1:1) by applying hydrothermal methods at 100–250 °C and at pH = 1, 4, 7, 9, and 13. FE-SEM/EDS was applied to investigate the as-samples' surface morphology. Fig. 3 depicts pH values ranging from 1 to 14; a delicate change could be observed in the reflection peaks derived for the crystal phases, which generated various compounds in the crystalline phase (see also Figs. S7–S9). These photocatalysts included BiOCl/BiOBr/BiOI, Bi_3O_4Cl/BiOBr/BiOI, $Bi_3O_4Cl/Bi_3O_4Br/Bi_4O_5I_2$, $Bi_{12}O_{17}Cl_2/Bi_3O_4Br/Bi_4O_5I_2$, $Bi_{12}O_{17}Cl_2/Bi_5O_7Br/Bi_5O_7I$, and $Bi_2O_3/Bi_5O_7Br/Bi_5O_7I$ (BiOCl/BiOBr/BiOI, $Bi_{12}O_{17}Cl_2/Bi_5O_7Br/Bi_5O_7I$, and $Bi_2O_3/Bi_5O_7Br/Bi_5O_7I$ in Fig. S7; BiOCl/BiOBr/BiOI, Bi_3O_4Cl/BiOBr/BiOI, $Bi_{12}O_{17}Cl_2$/BiOBr/$Bi_4O_5I_2$, $Bi_{12}O_{17}Cl_2/Bi_3O_4Br/Bi_5O_7I$, $Bi_{12}O_{17}Cl_2/Bi_5O_7Br/Bi_5O_7I$, and $Bi_2O_3/Bi_5O_7Br/Bi_5O_7I$ in Fig. S8; and BiOCl/BiOBr/BiOI, BiOCl/$Bi_4O_5Br_2$/BiOI, $Bi_3O_4Cl/Bi_4O_5Br_2/Bi_4O_5I_2$, $Bi_5O_7Br/Bi_4O_5I_2/Bi_5O_7I$, Bi_5O_7Br/Bi_5O_7I, and $Bi_2O_3/Bi_5O_7Br/Bi_5O_7I$ in Fig. S9) composites.

The samples had irregular shapes resembling sheets but the FE-SEM/EDS images in Fig. 3 reveal that for the samples obtained at 150 °C at various pH values, the corresponding morphology changed to pillars and irregular corner crystals, before changing to microirregular sheets and pillar crystals. Conversely, the FE-SEM/EDS images in Fig. S7 indicate that for the samples obtained at 100 °C at various pH values, the corresponding morphology changed from flower-like crystals and irregular sheets to irregular microsheets and irregular thin plates, to irregular pillar crystals, and finally to microrectangular and pillar crystals. Furthermore, the FE-SEM/EDS images in Fig. S8 reveal that for the samples obtained at 200 °C at various pH values, the corresponding morphology changed from macrothin sheet crystals and irregular superthin sheets to irregular square plates and irregular thin plates and microrectangular pillar crystals, to irregular pillar crystals, and finally to microrectangular pillar and irregular corner crystals. Finally, the FE-SEM/EDS images in Fig. S9 illustrate that for the samples obtained at a 250 °C at various pH values, the correspond-

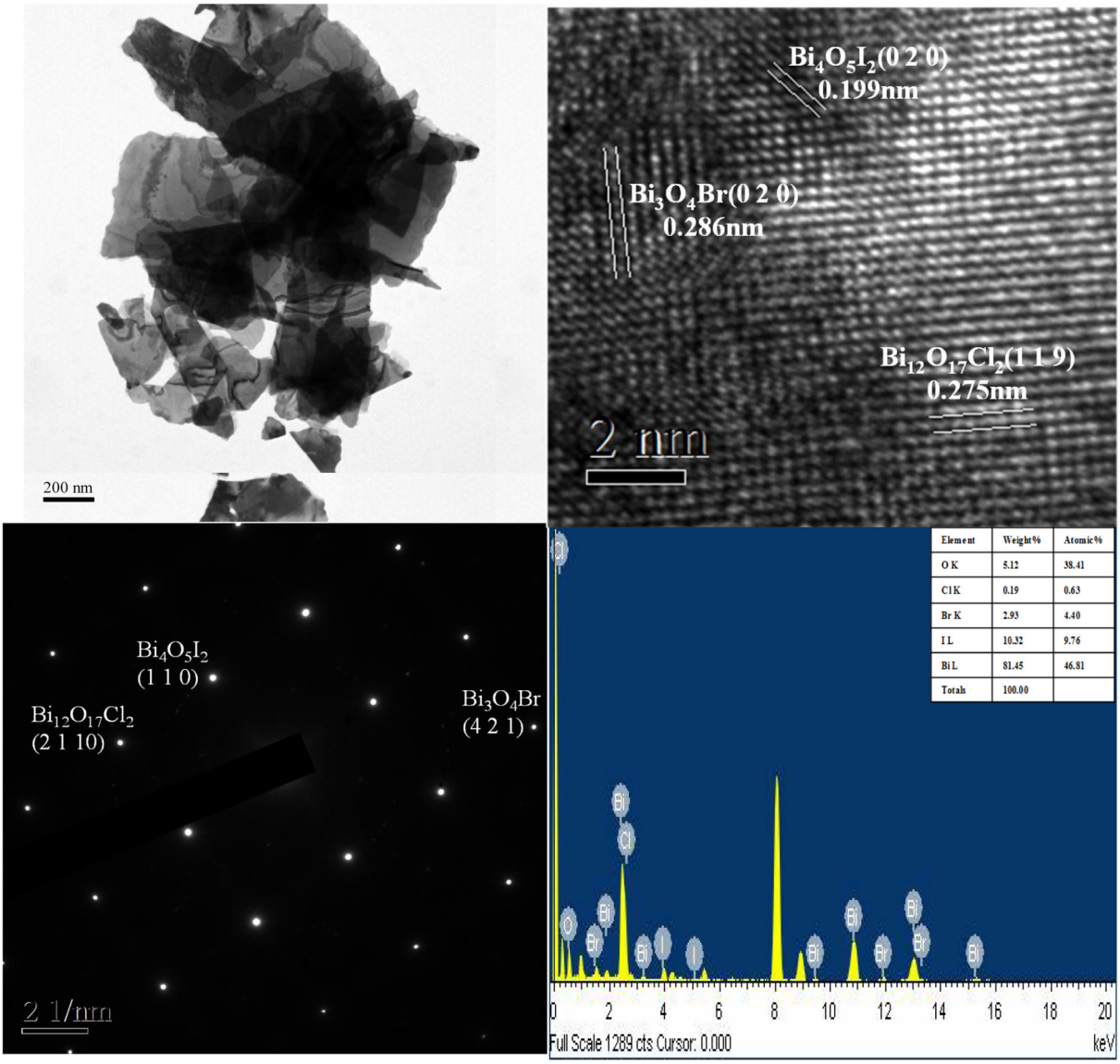

Fig. 2. FE-TEM images and EDS of BC1B1I1-10–150-12 ($Bi_{12}O_{17}Cl_2/Bi_3O_4Br/Bi_4O_5I_2$) sample by the hydrothermal autoclave method.

ing morphology changed from irregular thin multisheet crystals to irregular micromultisheets; to square multiplates, macro- and micro-rectangular pillar crystals, and irregular pillar crystals; and finally to macrorectangular multipillar and irregular corner crystals.

In the layered structure of any BiOX (X = F, Cl, Br, or I) substance, halogen atoms are positioned between layers of Bi_2O_2 [29]. Scholars believe that the internal electric fields that separate $Bi_2O_2^{2+}$ positive layers and negative halogen layers can achieve photogenerated electron–hole pair segregation effectively, consequently enhancing BiOX photocatalytic activity [30]. In this study, results derived from SEM-EDS and TEM-EDS demonstrated bismuth, chlorine, bromine, iodine, and oxygen to constitute the main elements within these samples, as observed at the various applied pH values (Table 3 and Fig. 2). For the samples, the calculated Cl (or Br, I) atomic ratios (%) were within 12.94–0.02 (or 11.42–0.25, 11.30–0.11), values that were ascribed to BiOCl, $Bi_4O_5Cl_2$, $Bi_{24}O_{31}Cl_{10}$, Bi_3O_4Cl, Bi_5O_7Cl, and $Bi_{12}O_{17}Cl_2$ (or BiOBr, $Bi_4O_5Br_2$, Bi_3O_4Br, Bi_5O_7Br, $Bi_{12}O_{17}Br_2$; BiOI, $Bi_4O_5I_2$, $Bi_7O_9I_3$, Bi_3O_4I, Bi_5O_7I) and Bi_2O_3 and their mixture phases, in contrast to the stoichiometric ratios (Bi:Cl and Bi:Br = 1, 2, 2.4, 3, 5, and 6, respectively; Bi:I = 1, 2, 2.3, and 5, respectively); the mentioned samples could be realized selectively through a convenient solution-based hydrothermal method.

3.1.3. XPS analysis

XPS was used to measure to execute purity measurement for the prepared samples. Fig. 4 illustrates the spectra, which are Bi 4f, O 1s, Cl 2p, Br 3d, and I 3d for the five $BiO_xCl_y/BiO_mBr_n/BiO_pI_q$ samples. Bi, O, Cl, Br, I, and C constituted the catalysts, as demonstrated by the transition peaks involving the orbitals for these spectra (Fig. 4a).

Furthermore, the typical binding energy was derived to be 158.2–159.0 eV for Bi $4f_{7/2}$ (Fig. 4b), indicating the oxidation state observed for bismuth to be trivalent. Each of the samples exhibited an extra spin–orbit doublet with a binding energy of 155.5–156.4 eV for Bi $4f_{7/2}$, which suggested some bismuth parts were in the $(+3-x)$ valence state and were reduced partially by the hydrothermal autoclave method to the lower valence state. Similarly, Chen et al. [12,24] have reported a chemical shift for Bi $4f_{7/2}$ in the range 2.4–2.6 eV, with the authors concluding that the formal oxidation state observed for $Bi^{(+3-x)}$ is attributable to

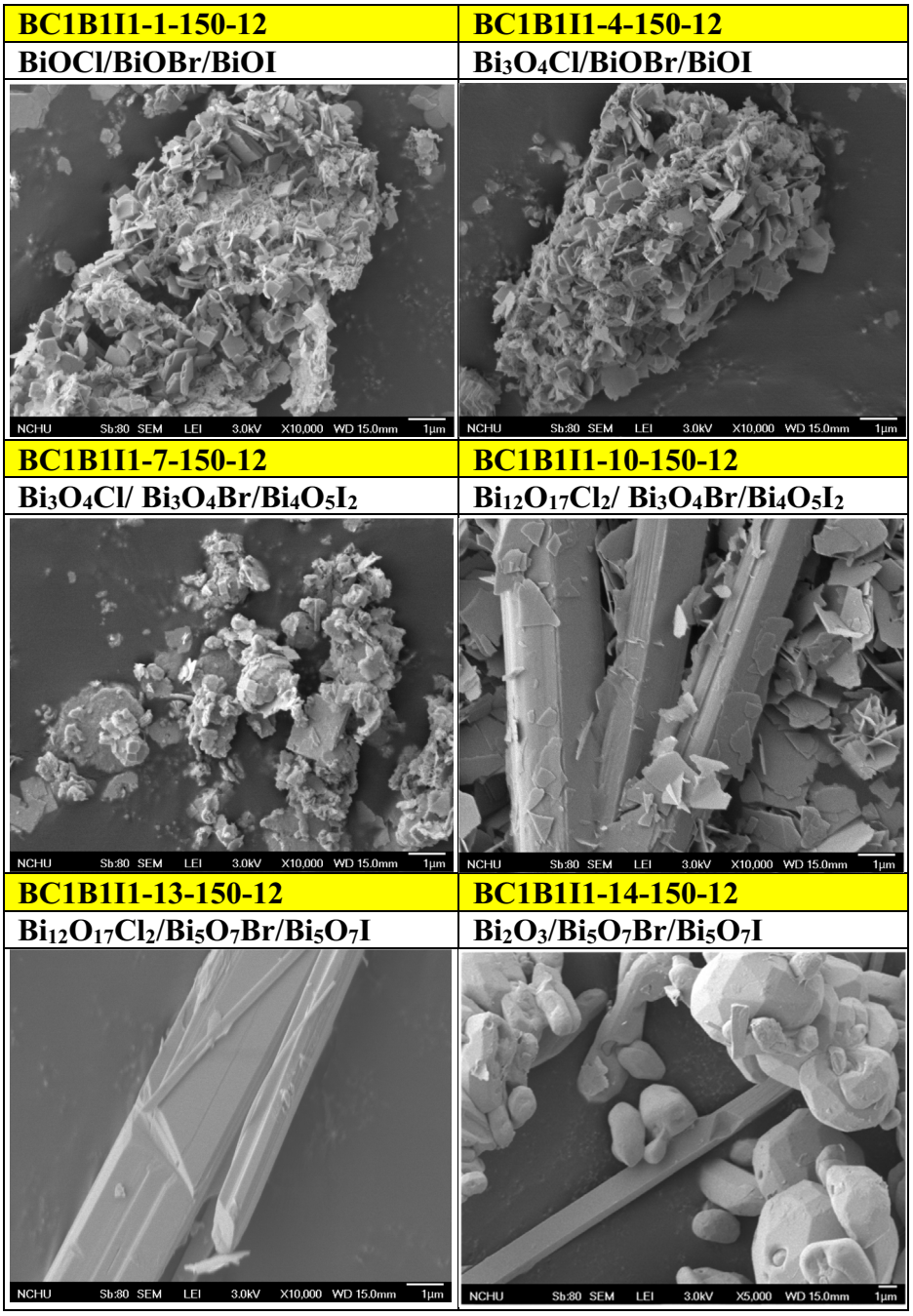

Fig. 3. SEM images of $BiO_xCl_y/BiO_mBr_n/BiO_pI_q$ prepared by the hydrothermal autoclave method at different pH values. (Molar ratio KCl:KBr:KI = 1:1:1, hydrothermal conditions: temp = 150 °C, pH = 1–14, time = 12 h).

the substoichiometric forms of Bi existing inside the Bi_2O_2 layer and to the establishment of a low oxidation state engendering oxygen vacancy in the crystal lattice. According to the characteristic binding energy, the oxidation state for the bond Bi^{+3}–O (or Bi^{+3}–Cl, Bi^{+3}–Br, Bi^{+3}–I) was trivalent; the presence of two extra spin–orbit doublets with the binding energy for Bi $4f_{7/2}$ suggested that certain parts of bismuth exist in the bond Bi^{+3-x}–O (or Bi^{+3}–Cl, Bi^{+3-x}–Br, Bi^{+3-x}–I) [12,24]. Fig. 4c presents the spectra for the O 1s region, as derived from high-resolution XPS; the presented data can be resolved into two peaks: a main peak (528.8 eV) ascribed to the bonds between Bi and O in the $Bi_2O_2^{2+}$ slabs of the BiOX layered structure and a secondary peak (529.9 eV) ascribed to the hydroxyl groups dwelling on the surface [12].

As shown in Fig. 4d, the binding energies that were observed for Cl $2p_{3/2}$ and Cl $2p_{1/2}$were 197.3 and 199.2 eV, respectively, corresponding to Cl existing in the monovalent oxidation state. Similarly, the binding energies that were determined for Br $3d_{5/2}$ and Br $3d_{3/2}$ were 67.9 and 68.9 eV, respectively (in Fig. 4e), corresponding to Br existing in the monovalent oxidation state. Finally, the binding energies that were noted for I $3d_{5/2}$ and I $3d_{3/2}$ were 618.5 and 630.0 eV, respectively, corresponding I in the monovalent oxidation state (Fig. 4f). According to the XPS results, possible bismuth oxychlorobromoiodide formation processes can be expressed in Eqs. (1)–(26); the presented findings are consistent with the previous results that were derived from the XRD and TEM analyses. Additionally, the results suggest chlorine, bromine,

Table 3
Physical and chemical properties of $BiO_xCl_y/BiO_mBr_n/BiO_pI_q$.

Catalyst code	EDS of atomic ratio(%)					Eg (eV)
	Bi	O	Cl	Br	I	
BC1B1I1-1-100-12	34.13	37.05	12.94	4.64	11.24	2.00
BC1B1I1-4-100-12	30.24	48.41	11.34	2.76	7.25	2.26
BC1B1I1-7-100-12	29.18	52.25	10.57	2.85	5.15	2.21
BC1B1I1-10-100-12	31.61	55.62	1.47	–	11.30	2.89
BC1B1I1-13-100-12	29.96	64.29	0.08	–	5.67	2.90
BC1B1I1-14-100-12	37.40	55.91	0.92	–	6.07	3.02
BC1B1I1-1-150-12	28.37	46.66	11.27	10.52	3.18	1.92
BC1B1I1-4-150-12	28.56	50.28	5.42	7.63	8.11	2.21
BC1B1I1-7-150-12	33.64	49.31	6.49	5.80	4.76	2.26
BC1B1I1-10-150-12	24.66	63.66	2.04	3.39	6.26	2.43
BC1B1I1-13-150-12	36.19	57.82	–	–	5.99	2.94
BC1B1I1-14-150-12	34.66	64.26	1.44	–	0.11	2.72
BC1B1I1-1-200-12	27.61	48.42	5.89	11.42	6.66	1.96
BC1B1I1-4-200-12	24.14	61.27	5.82	4.82	3.95	2.21
BC1B1I1-7-200-12	33.70	43.84	8.78	6.94	6.74	2.22
BC1B1I1-10-200-12	36.59	53.78	3.54	1.22	4.88	2.44
BC1B1I1-13-200-12	22.04	73.29	0.17	0.25	4.25	3.00
BC1B1I1-14-200-12	28.53	70.73	0.28	–	0.60	2.69
BC1B1I1-1-250-12	28.93	46.57	10.47	10.23	3.79	2.03
BC1B1I1-4-250-12	33.15	48.33	6.39	7.66	4.47	2.29
BC1B1I1-7-250-12	27.34	60.48	2.37	5.86	3.94	2.36
BC1B1I1-10-250-12	31.12	62.68	0.02	0.92	5.26	2.67
BC1B1I1-13-250-12	34.34	59.57	0.39	0.37	5.33	2.74
BC1B1I1-14-250-12	32.09	66.00	2.21	–	–	2.67

Catalyst code	XPS of atomic ratio(%)				
	Bi	O	Cl	Br	I
BC1B1I1-1-100-12	31.62	31.28	6.35	8.82	1.16
BC1B1I1-4-100-12	57.91	20.86	2.41	3.37	1.71
BC1B1I1-7-100-12	56.01	22.78	2.05	3.61	1.82
BC1B1I1-10-100-12	56.63	22.04	0.22	1.15	2.28
BC1B1I1-13-100-12	32.58	38.08	0.42	0.26	3.01

iodine, bismuth, and oxygen to be the main elements constituting the samples (Table 2). The Cl (or Br, I) atomic ratio (%) that was calculated for the samples was within 0.42–6.35 (or 0.26–8.82, 1.16–3.01), corresponding to the five $BiO_xCl_y/BiO_mBr_n/BiO_pI_q$ composites.

3.1.4. Optical absorption characteristics

The DR-UV data of multiple photocatalysts are given in Figs. 5 and S10–S12 of supplementary materials. BiOCl did not absorb any visible light and BiOBr absorbed a minuscule quantity of visible light. The observed absorption edge of BiOI spanned the visible light spectrum. In addition, the observed BiO_pI_q absorption edges exhibited the monotonic red-shift response of BiO_xCl_y. Given semiconductor absorption spectra, the E_g values of those semiconductors are calculable from the expression $\alpha h\nu = A(h\nu - E_g)^{n/2}$, where the values of n for BiOX (X = Cl, Br, or I) are 4 and 4, respectively [24,31]. The E_g value of $BiO_xCl_y/BiO_mBr_n/BiO_pI_q$ was discovered from the relation of $(\alpha h\nu)^{1/2}$ versus energy ($h\nu$), and was proven to be in the range from 1.92 to 2.94 eV (Figs. 5 and S10–S12). The intrinsic bandgap transition occurring between the valence and conduction bands, not impurity-level-induced transitions, can explain the steep shape and strong absorption that occurred in the visible region [32].

3.1.5. Adsorption–desorption isotherm, pore structure, and specific surface areas

Fig. 6 illustrates the nitrogen adsorption–desorption isotherms that were determined for $Bi_{12}O_{17}Cl_2/Bi_3O_4Br/Bi_4O_5I_2$. All samples' isotherms were determined to approximate Type IV isotherms along with a hysteresis loop observed at a pressure between 0.9 and 1.0 [15]. The hysteresis loop has a shape that resembles Type H3, which might indicate that particles resembling plates agglomerated to construct slit-like pores. Such agglomeration would be consistent with the samples' manifestation of self-assembled nanoplate-like morphology (Fig. 3) [15], and with the FE-SEM evidence that 3D hierarchical structures had self-assembled themselves from nanosheets or nanoplates. Additionally, Fig. 6 inset displays the corresponding $Bi_{12}O_{17}Cl_2/Bi_3O_4Br/Bi_4O_5I_2$ pore-size distribution (PSD). The PSD curves are trimodal for the $Bi_{12}O_{17}Cl_2/Bi_3O_4Br/Bi_4O_5I_2$ samples, indicating the presence of small (2–4 nm) and medium (10–50 nm) mesopores, as well as large (50–1100 nm) macropores. Because the nanosheets in the present research did not contain pores (Figs. 3 and S7–S9), the smaller mesopores may indicate the porosity of the nanosheets. The medium mesopores may be attributed to the pores that evolved between stacked nanosheets, whereas the large macropores can be attributed to the pores formed between nanosheets. These types of self-organized porous architectures have remarkable utility in photocatalysis because they can offer transport pathways for reactant and product molecules [33]. The pore volume and size of the composite sample were determined as 0.058491 cm^3/g and 37.1 nm, respectively.

The S_{BET} value determined from the BET isotherm of $Bi_{12}O_{17}Cl_2/Bi_3O_4Br/Bi_4O_5I_2$ was approximately 6.6072 m^2/g. Because the particles were relatively large, this range was noted to be below that of $Bi_4O_5I_2$ (8.08 m^2/g). A large S_{BET} and pore volume are associated with a high number of surface active sites and facilitate reactant transport, which tends to enhance the photocatalytic performance. Accordingly, the high photocatalytic activity of the composite may be explained by the large S_{BET} and pore volume that were derived for $Bi_{12}O_{17}Cl_2/Bi_3O_4Br/Bi_4O_5I_2$. The extant nanosheet structure affords highly efficient paths for transporting reactants and a high number of active sites for executing photocatalytic reactions, in addition to enhancing the efficient harvest of photoenergy and

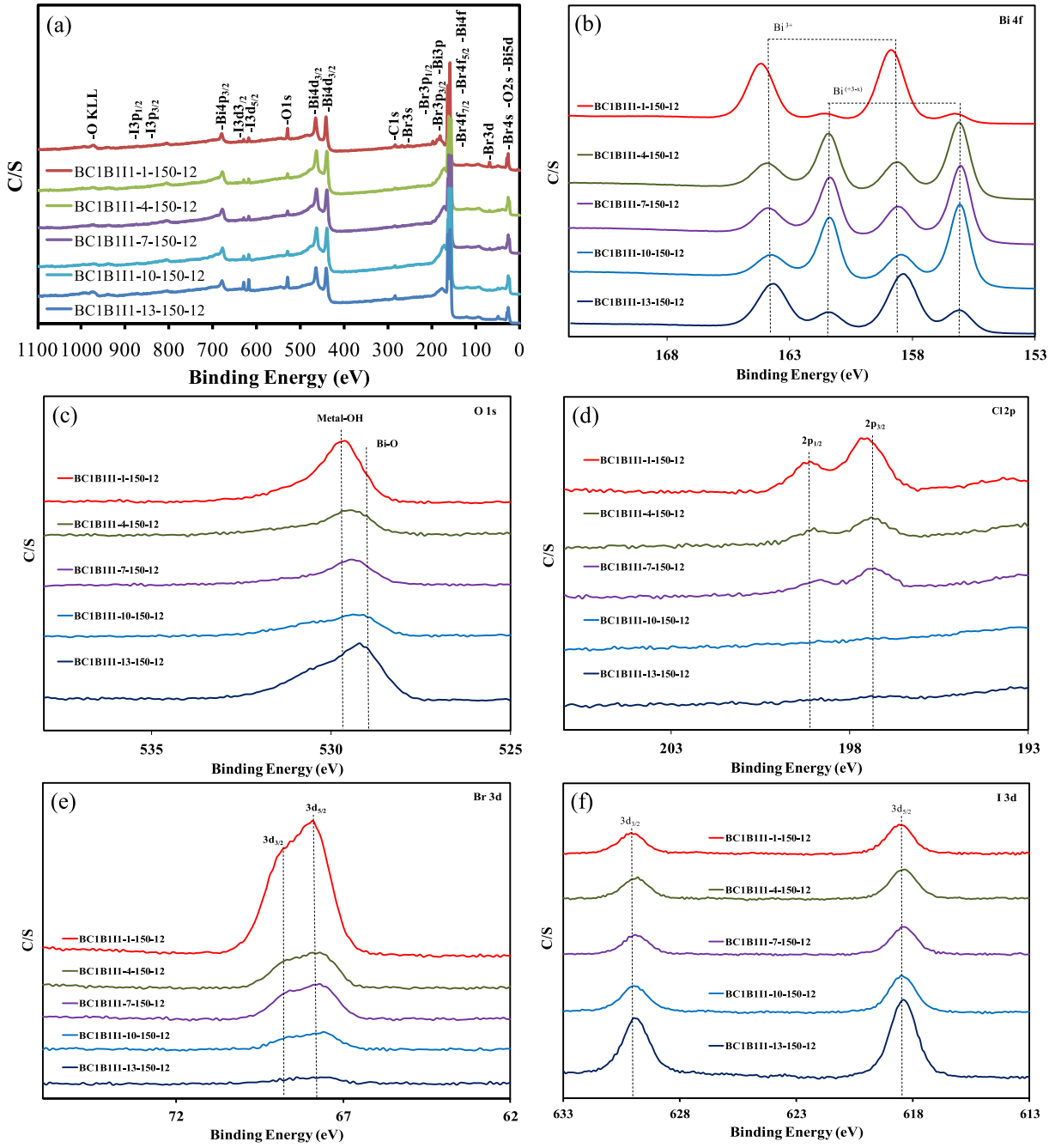

Fig. 4. High resolution XPS spectra of as-prepared $BiO_xCl_y/BiO_mBr_n/BiO_pI_q$ samples under different pH values. (a) total survey; (b) Bi 4f; (c) O 1s; (d) Cl 2p; (e) Br 3d; (f) I 3d. (Molar ratio KCl:KBr:KI = 1:1:1).

segregation of electron–hole pairs, the ultimate outcome of which is enhanced photocatalytic activity.

3.2. Photocatalytic activity

Fig. 7 depicts the variations of the UV–Vis spectra that were observed during HBA and CV photodegradation executed in aqueous $Bi_{12}O_{17}Cl_2/Bi_3O_4Br/Bi_4O_5I_2$ dispersions under irradiation provided by visible light. After 24 h of irradiation, approximately 98.3% of the HBA had decomposed and nearly 99.9% of the CV had degraded. During irradiation, the characteristic CV dye absorption band at approximately 588 nm was noted to decline rapidly with slight hypsochromic shifts (555 nm), but the results did not reveal any additional absorption band nor did they signify a band in the UV range ($\lambda > 200$ nm); this thus suggests that a series of *N*-demethylated intermediates may have formed, and the entire conjugated chromophore structure of the CV dye may have cleaved. Additional irradiation decreased the absorption band at 555 nm; however, no additional wavelength shift was observed, implying the band existing at 555 nm to be a fully *N*-demethylated product of the CV dye [18,24].

In Fig. 8 and in Figs. S13–S21 of Supplementary Materials, the efficiency of the degradation process is expressed as a function of the reaction time. The use of $BiO_xCl_y/BiO_mBr_n/BiO_pI_q$ resulted in a significant enhancement of the removal efficiency. After 24 h of irradiation, the $BiO_xCl_y/BiO_mBr_n/BiO_pI_q$ composites demonstrated

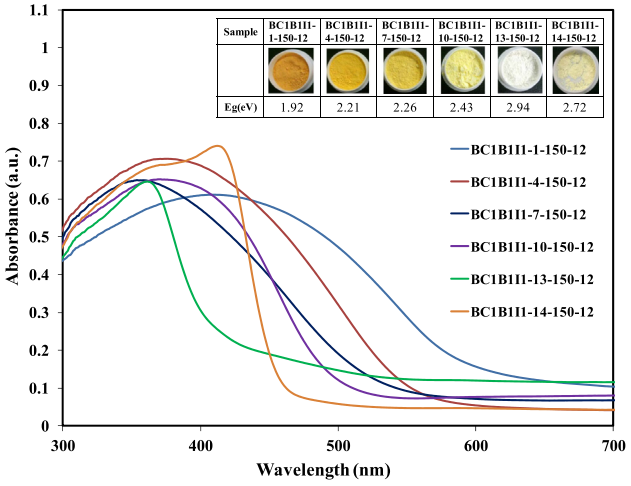

Fig. 5. UV–vis absorption spectra of as-prepared $BiO_xCl_y/BiO_mBr_n/BiO_pI_q$ samples under different pH values.

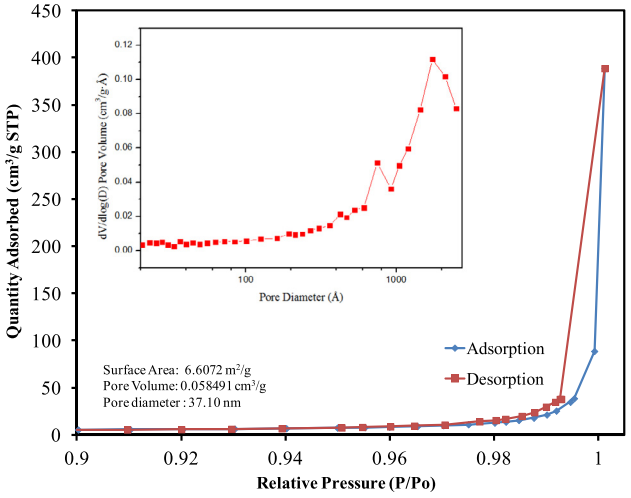

Fig. 6. N_2 adsorption-desorption isotherm distribution curves for enlarged view and the pore distribution curves (inset) of as-prepared of $Bi_{12}O_{17}Cl_2/Bi_3O_4Br/Bi_4O_5I_2$.

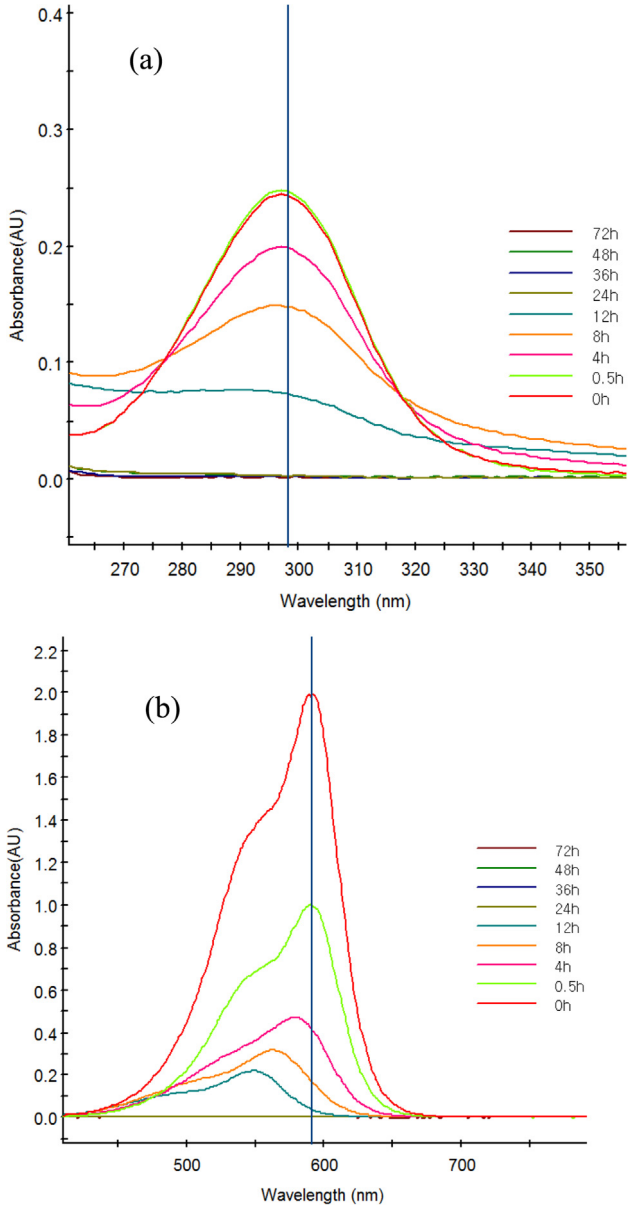

Fig. 7. Temporal UV–vis adsorption spectral changes during the photocatalytic degradation of (a) HBA and (b) CV over aqueous $Bi_{12}O_{17}Cl_2/Bi_3O_4Br/Bi_4O_5I_2$ under visible light irradiation.

superior photocatalytic performance, with the removal efficiency observed for HBA reaching 99%. For further comprehending the reaction kinetics underlying HBA degradation, this study applied an apparent pseudo-first-order model [24] in the experiments: $\ln(C_o/C) = kt$. When a first-order linear fit was applied to the evidence from Tables 4 and 5, the k value of $Bi_{12}O_{17}Cl_2/Bi_3O_4Br/Bi_4O_5I_2$ for HBA degradation and of the $Bi_3O_4Cl/BiOBr/BiOI$ for CV degradation were obtained at a maximum degradation rate of $1.78 \times 10^{-1}\ h^{-1}$ and $3.35 \times 10^{-1}\ h^{-1}$, respectively. These values notably exceeded those of other composites synthesized in this study, indicating that the $Bi_{12}O_{17}Cl_2/Bi_3O_4Br/Bi_4O_5I_2$ for HBA degradation and the $Bi_3O_4Cl/BiOBr/BiOI$ for CV degradation were much more effective photocatalysts.

Table 5 presents a list of the single, binary, and ternary bismuth oxyhalides, demonstrating that among the samples in this study, the ternary bismuth oxyhalide exhibited the highest photocatalytic activity; moreover, the table reveals photocatalytic activity variations to be associated with the $BiO_xCl_y/BiO_mBr_n/BiO_pI_q$ composites. The photocatalytic activity enhancement observed for the $BiO_xCl_y/BiO_mBr_n/BiO_pI_q$ materials may be attributed to the synergistic effect of the formation of heterojunctions, the layered structure, the high BET surface area, and a low-energy band structure. If no photocatalysts were present under visible light irradiation, HBA and CV could not be degraded; thus, the superior $BiO_xCl_y/BiO_mBr_n/BiO_pI_q$ photocatalytic activity might be attributed to its efficient visible light utilization and remarkably effective electron–hole pair segregation within the composites.

Furthermore, the used catalyst was recycled to discover that $Bi_{12}O_{17}Cl_2/Bi_3O_4Br/Bi_4O_5I_2$ is a highly durable composite. After each cycle, centrifugation was performed so that the catalyst could be collected. Removing HBA (or CV) in the fifth cycle engendered no evident photocatalytic activity decline; even in the 10th cycle, the photocatalytic activity decline observed was only 1% (Fig. 9a). The used $Bi_{12}O_{17}Cl_2/Bi_3O_4Br/Bi_4O_5I_2$ was also examined using XRD; but no difference was detectable between the as-prepared and the used samples (Fig. 9b); consequently, the photostability of $Bi_{12}O_{17}Cl_2/Bi_3O_4Br/Bi_4O_5I_2$ is remarkably high.

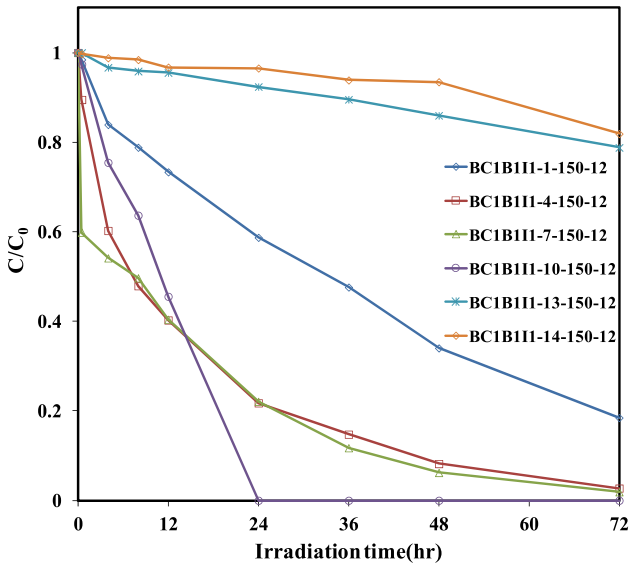

Fig. 8. Photodegradation of BHA as a function of irradiation time over different $BiO_xCl_y/BiO_mBr_n/BiO_pI_q$ photocatalysts. Molar ratio KCl:KBr:KI = 1:1:1.

3.3. Photodegradation mechanisms of HBA and CV

Scholars have proposed three reaction mechanisms for organic or dye photodegradation using a semiconductor: (1) photolysis, (2) photocatalysis, and (3) dye photosensitization [34]. Photolysis entails the reaction of a photoinduced electron existing on the induced dye directly with O_2 to yield a single oxygen atom; the obtained oxygen atom can serve as an oxidant in pure dye photolysis [34,35]. This study performed blank experiments, but the study observed neither HBA nor CV degradation by photolysis under visible light; because both materials had stable structures, negligible decomposition occurred by photolysis.

The irradiating light applied in dye photosensitization causes electron emission from the dye, and a catalyst absorbs that dye; those electrons are transferred to the conduction band of the catalyst. Those transferred electrons then react with O_2 to generate the oxidant $O_2^{\cdot-}$ [31,34]. In the experiments, minor changes in the HBA or CV concentrations between various samples were detectable before the photocatalytic reactions began; those minor changes were evident within 30 min of the dark adsorption experiments. In dye photosensitization, these types of minor HBA or CV adsorption on the catalyst benefit charge carrier transfer between the dye and the catalyst surfaces. One might speculate that the presence of $BiO_xCl_y/BiO_mBr_n/BiO_pI_q$ composites does not obstruct photosensitization processes; thus, it might be possible that the photosensitization mechanism could be involved in CV decomposition.

Whereas photocatalysts produce electron–hole pairs directly after illumination in the photocatalytic process, their photocatalytic efficiency mainly hinges on the recombination rate or the lifetime of the photogenerated electron–hole pairs. The more rapidly they recombine, the faster the chemical reactions are. Cl spectra were thus employed in this study to explore the photogenerated electron–hole pairs' recombination rate; they were also measured to explore the photogenerated carriers' separation capacity in the $BiO_xCl_y/BiO_mBr_n/BiO_pI_q$ heterostructures (Fig. 10). The as-prepared materials exhibited a weak emission peak of approximately 396–467 nm, possibly engendered by the direct electron–hole recombination of band transitions. The characteristic emission peak at the lowest intensity range of 396–467 nm for the $BiO_xCl_y/BiO_mBr_n/BiO_pI_q$ evinces strikingly inhibited recombination of the photogenerated charge carriers. Conversely, efficient segregation might prolong the charge carrier lifespan and fortify the effectiveness of interfacial charge transfers to the adsorbed substrates, to the great benefit of the photocatalytic activity [12]. The PL intensities observed for the $BiO_xCl_y/BiO_mBr_n/BiO_pI_q$ composites were relatively low, as depicted in Fig. 10, suggesting that their electron–hole recombination rate was meager, which also results in higher photocatalytic activity (Fig. 8, Tables 4 and 5). Moreover, the PL results confirm that the composites are crucial to hindering electron–hole recombination, explaining why the $BiO_xCl_y/BiO_mBr_n/BiO_pI_q$ composites could offer increasing photocatalytic performance.

Some primary reactive species, notably $HO^{\cdot}$, h^+, $O_2^{\cdot-}$, $H^{\cdot}$, and $^1O_2$, can develop in the photocatalytic degradation processes of UV–Vis/semiconductor systems [23,25,36]. Yin et al. published a pathway for the manifestation of active hydroxyl radicals ($^{\cdot}OH$) and $^1O_2$ on the surface of Au/ZnO to degrade methylene blue and salicylic acid

Table 4
The pseudo-first-order rate constants for the degradation of HBA with $BiO_xCl_y/BiO_mBr_n/BiO_pI_q$ photocatalysts under visible light irradiation.

Cl : Br : I = 1 : 1 : 1												
Temperature (°C)	pH											
	1		4		7		10		13		14	
	$k(h^{-1})$	R^2	$k(h^{-1})$	R^2	$k(h^{-1})$	R^2	$k(h^{-1})$	R^2	$k(h^{-1})$	R^2	$k(h^{-1})$	R^2
100	0.018	0.989	0.085	0.981	0.122	0.996	0.091	0.952	0.008	0.989	0.003	0.942
150	0.024	0.946	0.073	0.952	0.076	0.952	0.178	0.951	0.005	0.982	0.002	0.938
200	0.031	0.998	0.061	0.951	0.067	0.958	0.175	0.950	0.005	0.981	0.001	0.906
250	0.026	0.951	0.037	0.961	0.034	0.991	0.006	0.971	0.018	0.972	0.002	0.912
Temperature (°C) = 150												
Molar ratio	pH											
	1		4		7		10		13		14	
	$k(h^{-1})$	R^2	$k(h^{-1})$	R^2	$k(h^{-1})$	R^2	$k(h^{-1})$	R^2	$k(h^{-1})$	R^2	$k(h^{-1})$	R^2
1 : 1 : 1	0.024	0.946	0.073	0.952	0.076	0.952	0.178	0.951	0.005	0.982	0.002	0.938
3 : 1 : 1	0.015	0.964	0.055	0.816	0.143	0.936	0.039	0.950	0.004	0.984	0.002	0.831
1 : 3 : 1	0.046	0.990	0.092	0.954	0.016	0.999	0.028	0.974	0.001	0.919	0.002	0.872
1 : 1 : 3	0.013	0.864	0.065	0.988	0.115	0.968	0.093	0.924	0.005	0.981	0.004	0.983

Table 5
The pseudo-first-order rate constants for the degradation of HBA and CV with $BiO_xCl_y/BiO_mBr_n/BiO_pI_q$ photocatalysts under visible light irradiation.

Catalyst code	HBA		CV	
	K (h^{-1})	R^2	K (h^{-1})	R^2
$Bi_{12}O_{17}Cl_2$	0.023	0.812	0.015	0.891
Bi_3O_4Br	0.027	0.985	0.035	0.976
$Bi_4O_5I_2$	0.032	0.998	0.078	0.993
$Bi_{12}O_{17}Cl_2/Bi_3O_4Br$	0.028	0.947	0.046	0.990
$Bi_{12}O_{17}Cl_2/Bi_4O_5I_2$	0.166	0.937	0.186	0.993
$Bi_3O_4Br/Bi_4O_5I_2$	0.156	0.970	0.097	0.995
BiOCl/BiOBr/BiOI	0.024	0.946	0.088	0.906
Bi_3O_4Cl/BiOBr/BiOI	0.073	0.952	0.335	0.963
$Bi_3O_4Cl/Bi_3O_4Br/Bi_4O_5I_2$	0.076	0.952	0.100	0.921
$Bi_{12}O_{17}Cl_2/Bi_3O_4Br/Bi_4O_5I_2$	0.178	0.951	0.102	0.997
$Bi_{12}O_{17}Cl_2/Bi_5O_7Br/Bi_5O_7I$	0.005	0.982	0.010	0.878
$Bi_5O_7Br/Bi_5O_7I/Bi_2O_3$	0.002	0.938	0.006	0.890

[37]. Shenawi-Khalil et al. suggested that $O_2^{-}\cdot$ and h^+ oxidation played the dominant roles in rhodamine-B photodegradation by $yBiO(Cl_xBr_{1-x})$–$(1-y)$ bismuth oxide hydrate under visible light [38]. Notably, Cao et al. determined hydroxyl radicals and direct holes to act as the primary reactive species in methyl orange degradation by BiOI/BiOBr spheres under irradiation provided by visible light [31], whereas He et al. reported ·OH, $^1O_2$, and h^+ to be the three main active species throughout the degradation process by ZnS [39]. Wang et al. argued that the ·OH radical was produced through a multistep reduction of $O_2^{-}\cdot$ [15].

Notably, the hydroxyl radical HO· might only be generated through the $e^- \rightarrow O_2^{-}\cdot \rightarrow H_2O_2 \rightarrow$ ·OH route, whereas the ·OH radical is generated through a multistep $O_2^{-}\cdot$ reduction. In a Bi^{3+} valence band, holes generated through photoexcitation were considered to be Bi^{5+} [40]; however, the standard redox potential of Bi^{5+} and Bi^{3+} was more negative than that of OH· and that of OH^- [41]. In this context, one might not expect photogenerated holes on the surface of bismuth oxyhalides to react with OH^-/H_2O to form ·OH; thus, in both species, rhodamine decomposition [39] can be ascribed to a direct reaction with the photogenerated holes or with a superoxide radical (generated by an excited electron). Zhu et al. argued that photocatalytic experiments in the presence of N_2 and a radical scavenger indicate that ·OH and $O_2^{-}\cdot$ are the two main active species in the degradation process [42]. Dimitrijevic et al. [36] proposed that dissociated water on the surface of TiO_2 and in subsequent molecular layers had three roles: (1) preventing electron–hole recombination and thus acting as a stabilizing influence on charges, (2) giving electrons (reacting with photogenerated holes to produce ·OH radicals), and (3) accepting electrons (forming H atoms in reaction to photogenerated electrons with protons on the surface of $—OH_2^+$). According to previous studies [17], the dominant active oxygen species created through direct oxidation and photocatalytic reactions are $^1O_2$ and ·OH radicals, respectively. In this type of visible-light-induced semiconductor system, hydroxylated compounds were identified for the photocatalytic degradation of CV [12]. Thus, we proposed that the formation of ·OH is much less probable than the formation of $O_2^{-}\cdot$.

To investigate the impact of the active species in the photocatalytic reaction, a series of quenchers were applied to scavenge the relevant active species, in a method resembling the photocatalytic activity test. ·OH, $O_2^{-}\cdot$, $^1O_2$, and h^+ were examined by adding 1.0 mM benzoquinone (BQ, a quencher of $O_2^{-}\cdot$) [43], 1.0 mM isopropanol (IPA, a quencher of ·OH) [44], 1.0 mM ammonium oxalate (AO, a quencher of h^+) [45], and 1.0 mM sodium azide (SA, a quencher of $^1O_2$) [46], respectively. As illustrated in Fig. 11a, the degradation efficiency of BQ quenching declined more than those of IPA and AO, but the photocatalytic degradation of HBA was not influenced by the addition of SA. Thus, the quenching caused by various scavengers revealed that the reactive $O_2^{-}\cdot$ was crucial, whereas the ·OH and h^+ played minor roles in HBA degradation; furthermore, the ·OH radical was created through a multistep reduction of $O_2^{-}\cdot$.

As indicated in Fig. 11b and 11c, when the reaction was executed in the dark, no EPR signals were noted. However, when the reaction process was conducted under irradiation provided by visible light, intensity signals corresponding to the characteristic peak of DMPO-$O_2^{-}\cdot$ adducts (Fig. 11b) were noted, and prolonging the reaction time resulted in a gradual increase in the intensity; conversely, when the reaction process was conducted under irradiation provided by visible light, DMPO-·OH adducts (Fig. 11c) were not noted, and prolonging the reaction time resulted in a gradual reduction in the intensity. This suggests that the $O_2^{-}\cdot$ (main active species) and ·OH (minor active species) were formed in the presence of $BiO_xCl_y/BiO_mBr_n/BiO_pI_q$ and oxygen under irradiation provided by visible light. As shown in Fig. 11a, 1O2 can be negligible, but $O_2^{-}\cdot$ is a main active species and ·OH and h^+ are minor active species in HBA degradation. Moreover, dissolved oxygen can trap the photogenerated electrons to and from $O_2^{-}\cdot$, a phenomenon that promotes HBA decomposition. This photocatalytic mechanism is consistent with the preceding $BiO_xCl_y/BiO_mBr_n/BiO_pI_q$ band structure analysis and may be further confirmed using the EPR technique [27].

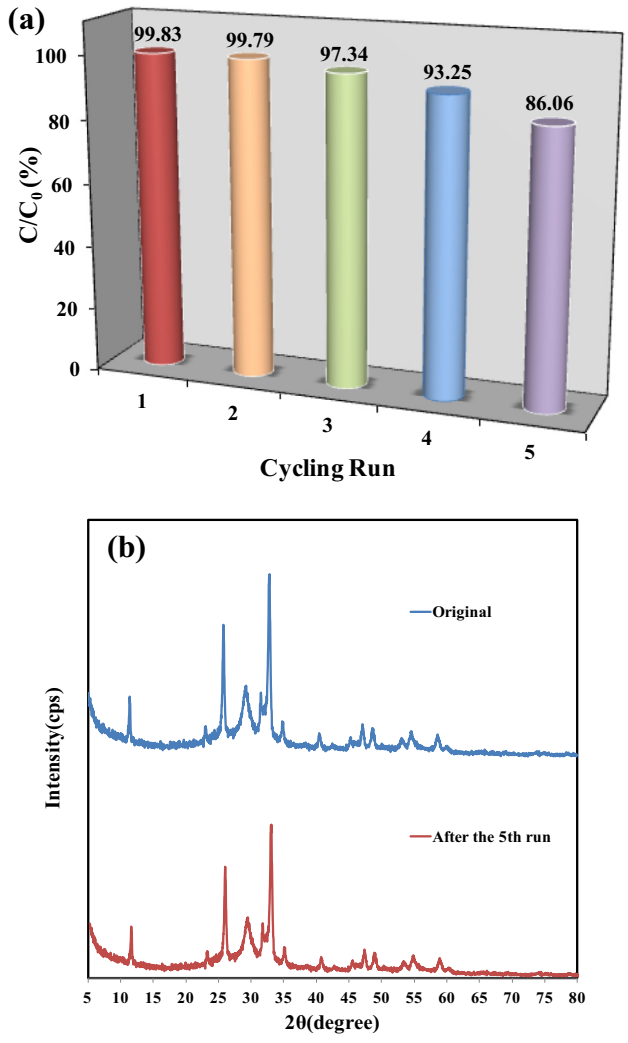

Fig. 9. (a) Cycling runs in the photocatalytic degradation of HBA in the presence of $Bi_{12}O_{17}Cl_2/Bi_3O_4Br/Bi_4O_5I_2$; (b) XRD of powder sample before and after the degradation reaction.

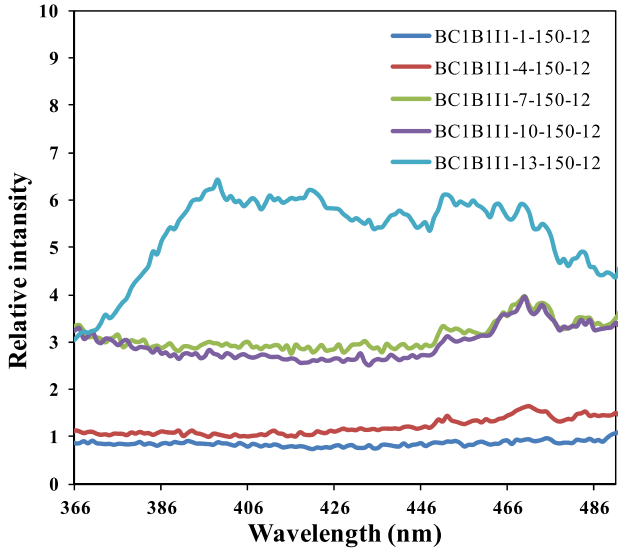

Fig. 10. Photoluminescence spectra of $BiO_xCl_y/BiO_mBr_n/BiO_pI_q$.

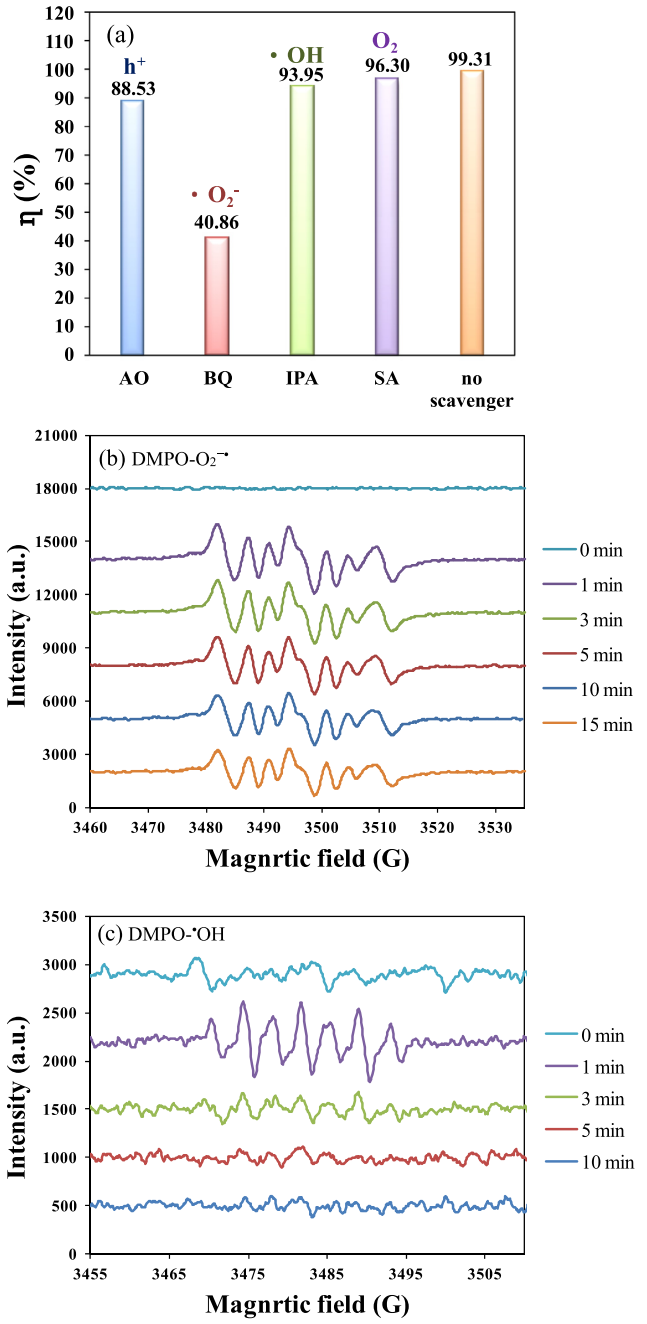

Fig. 11. (a) The dye concentration during photodegradation as a function of irradiation time observed in $Bi_{12}O_{17}Cl_2/Bi_3O_4Br/Bi_4O_5I_2$ under the addition of different scavengers: SA, IPA, AQ, and BQ; (b) (c) DMPO spin-trapping EPR spectra for DMPO-O_2^{-}· and DMPO-·OH under visible light irradiation with $Bi_{12}O_{17}Cl_2/Bi_3O_4$-$Br/Bi_4O_5I_2$.

The photocatalytic process proceeds concurrently to photosensitization (Fig. 12a). Visible light irradiation produces these cycles as long as the light is maintained [21]; when the photooxidation process has been established by the passing of multiple cycles, the degradation of HBA by the formed oxidant species can be formalized in terms of Eqs. (27)–(29):

$$HBA + h^+ \rightarrow HBA^{+\bullet} \rightarrow \text{degraded compounds} \quad (27)$$

$$HBA + OH^{\bullet}/O_2^{-\bullet} \rightarrow \text{degraded compounds} \quad (28)$$

$$HBA^{+\bullet} + OH^{\bullet}/O_2^{-\bullet} \rightarrow \text{degraded compounds} \quad (29)$$

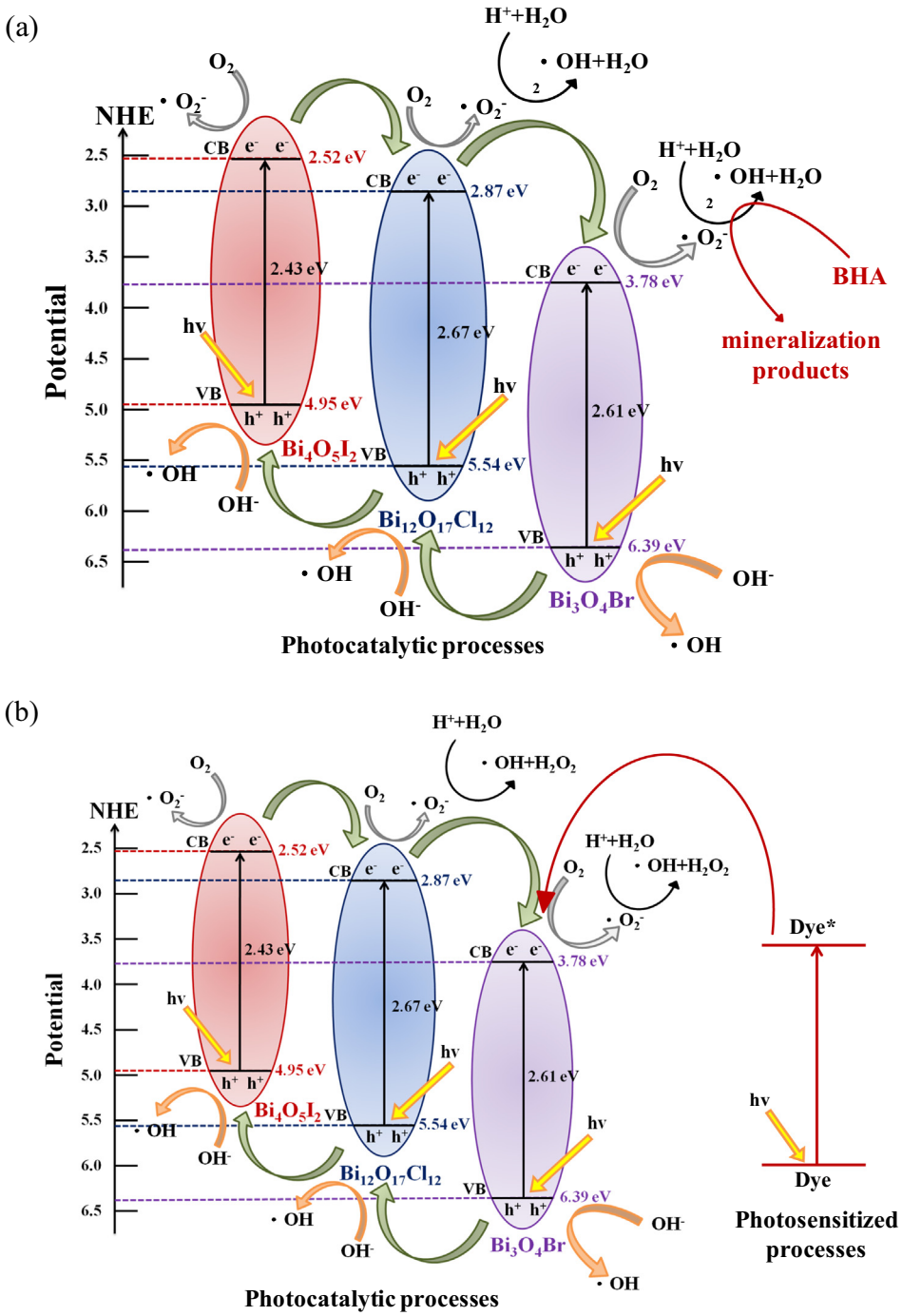

Fig. 12. The band structure diagram of $BiO_xCl_y/BiO_mBr_n/BiO_pI_q$ nanocomposites and the possible charge separation processes. (a) BHA (b) CV.

The dye resulting from the photosensitization process exhibits a dye-sensitized degradation mechanism [18,23,42]. The determined photocatalytic degradation results from CV photodegradation through the photocatalytic pathway of CV-photosensitized $BiO_xCl_y/BiO_mBr_n/BiO_pI_q$. CV enters an excited electronic state (CV^*) when a visible photon is absorbed, from which an electron is transferred into the $BiO_xCl_y/BiO_mBr_n/BiO_pI_q$ conduction band:

$$CV + h\nu \rightarrow CV^* \quad (30)$$

$$CV^* + BiO_xCl_y/BiO_mI_n/BiO_pI_q \rightarrow CV^{+\bullet} + BiO_xCl_y/BiO_mI_n/BiO_pI_q\ (e^-) \quad (31)$$

$$O_2 + e^- \rightarrow O_2^{-\bullet} \quad (32)$$

The electron generates active oxygen species after reaching the $BiO_xCl_y/BiO_mBr_n/BiO_pI_q$ conduction band, engendering CV degradation. In addition to CV photodegradation through $BiO_xCl_y/BiO_mBr_n/BiO_pI_q$-mediated and photosensitized processes, the enhanced photocatalytic activity can be clearly attributed to another photocatalytic pathway. Despite the concurrent execution of the photocatalytic and photosensitized processes (Fig. 12b), O_2^- results from the reaction of O_2 with photogenerated and photosensitized e^- on the surface of the photocatalyst, whereas $^{\cdot}OH$ results from the O_2^-–H^+ and h^+–OH^- (or H_2O) reactions [18,24].

4. Conclusions

A series of ternary $BiO_xCl_y/BiO_mBr_n/BiO_pI_q$ photocatalysts were synthesized and characterized, thus constituting the first systematic synthetic study conducted on $BiO_xCl_y/BiO_mBr_n/BiO_pI_q$ based on controlled hydrothermal synthesis. Control experiments were designed and executed to investigate the pH, temperature, and KCl: KBr: KI molar ratio effects on the hydrothermal reactions involved in composite synthesis. The synthesis methods demonstrated herein can elucidate future technological applications through a controlled hydrothermal condition. The augmented photocatalytic activities of $BiO_xCl_y/BiO_mBr_n/BiO_pI_q$ could be ascribed to the heterojunction formation between BiO_xCl_y, BiO_mI_n, and BiO_pI_q, which could effectively suppress photoinduced electron–hole pair recombination. Thus, photocatalytic activity enhancements observed for $BiO_xCl_y/BiO_mBr_n/BiO_pI_q$ could be ascribed to the synergistic effect of the high BET surface area, layered structure, heterojunction formation, and low-energy band structure. Both photocatalysis and photosensitization concurrently advanced CV degradation, but photocatalysis was the sole process in HBA degradation; $O_2^{-\cdot}$ was the main active species and $^{\cdot}OH$ and h^+ were the minor active species in the photocatalytic process. The reaction mechanisms explained herein can elucidate future technological applications of dye degradation through the use of visible light.

Acknowledgments

This research was supported by the Ministry of Science and Technology of the Republic of China (MOST-106-2113-M-142-001). We acknowledge Wallace Academic Editing for editing this manuscript.

Appendix A. Supplementary material

Supplementary data associated with this article can be found, in the online version, at https://doi.org/10.1016/j.jcis.2018.04.097.

References

[1] Tauxe-Wuersch, L.F. De Alencastro, D. Grandjean, J. Tarradellas, Water Res. 39 (2005) 1761–1772.
[2] Q. Bu, B. Wang, J. Huang, S. Deng, G. Yu, Hazard J. Mater. 262 (2013) 189–211.
[3] M. Berk, O. Dean, H. Drexhage, J.J. McNeil, S. Moylan, A. O'Neil, M. Maes, BMC Med. 11 (2013) 74.
[4] A.C. Vlot, D.M.A. Dempsey, D.F. Klessig, Annu. Rev. Phytopathol. 47 (2009) 177–206.
[5] A.J. Langstieh, P. Verma, A.K. Thakur, S.S. Chatterjee, V. Kumar, Pharmacologia 5 (2014) 326–338.
[6] A.N. Rao, B. Sivasankar, V. Sadasivam, Hazard J. Mater. 166 (2009) 1357–1361.
[7] S.S. Shinde, C.H. Bhosale, K.Y. Rajpure, Mol J. Catal. A: Chem. 347 (2011) 65–72.
[8] B. Réti, Z. Major, D. Szarka, T. Boldizsár, E. Horváth, A. Magrez, L. Forró, A. Dombi, K. Hernádi, J. Mol. Catal. A: Chem. 414 (2016) 140–147.
[9] K.T. Ranjit, I. Willner, S.H. Bossmann, A.M. Braun, Catal J. 204 (2001) 305–313.
[10] L.M. Lewis, G.L. Indig, Photochem. J. Photobiol. B: Biolog. 67 (2002) 139–148.
[11] B.P. Cho, T. Yang, L.R. Blankenship, J.D. Moody, M. Churchwell, F.A. Bebland, S.J. Culp, Chem. Res. Toxicol. 16 (2003) 285–294.
[12] Y.R. Jiang, H.P. Lin, W.H. Chung, Y.M. Dai, W.Y. Lin, C.C. Chen, J. Hazard. Mater. 283 (2015) 787–805.
[13] F. Chen, P. Fang, Y. Gao, Z. Liu, Y. Liu, Y. Dai, Chem. Eng. J. 204–206 (2012) 107–113.
[14] W.L. Lee, J.S. Lin, J.L. Chang, J.Y. Chen, M.C. Cheng, C.C. Chen, J. Mol. Catal. A: Chem. 361–362 (2012) 80–90.
[15] J. Wang, Y. Yu, L. Zhang, Appl. Catal. B: Environ. 136–137 (2013) 112–121.
[16] W. Zhao, F. Liang, Z.M. Jin, X.B. Shi, P.H. Yin, X.R. Wang, C. Sun, Z.Q. Gao, L.S. Liao, J. Mater. Chem. A 2 (2014) 13226–13231.
[17] K. Yu, S. Yang, C. Liu, H. Chen, H. Li, C. Sun, S.A. Boyd, Environ. Sci. Technol. 46 (2012) 7318–7326.
[18] S.Y. Chou, C.C. Chen, L.W. Chen, Y.M. Dai, J.H. Lin, W.W. Lee, RSC Adv. 6 (2016) 33478–33491.
[19] C.T. Yang, W.W. Lee, H.P. Lin, Y.M. Dai, H.T. Chi, C.C. Chen, RSC Adv. 6 (2016) 40664–40675.
[20] H.P. Lin, C.C. Chen, W.W. Lee, Y.Y. Lai, J.Y. Chen, Y.Q. Chen, J.Y. Fu, RSC Adv. 6 (2016) 2323–2336.
[21] W.W. Lee, C.S. Lu, C.W. Chuang, Y.J. Chen, J.Y. Fu, C.W. Siao, C.C. Chen, RSC Adv. 5 (2015) 23450–23463.
[22] K. Li, W.W. Lee, C.S. Lu, Y.M. Dai, S.Y. Chou, M.C. Wang, C.C. Chen, J. Taiwan Inst. Chem. Eng. 45 (2014) 2688–2697.
[23] S.T. Huang, Y.R. Jiang, S.Y. Chou, Y.M. Dai, C.C. Chen, J. Mol. Catal. A: Chem. 391 (2014) 105–120.
[24] Y.R. Jiang, S.Y. Chou, J.L. Chang, S.T. Huang, H.P. Lin, C.C. Chen, RSC Adv. 5 (2015) 30851–30860.
[25] X. Xiao, R. Hao, M. Liang, X. Zuo, J. Nan, L. Li, W. Zhang, J. Hazard. Mater. 233–234 (2012) 122–130.
[26] S. Shenawi-Khalil, V. Uvarov, Y. Kritsman, E. Menes, I. Popov, Y. Sasson, Catal. Commun. 12 (2011) 1136–1141.
[27] X. Xiao, C. Xing, G. He, X. Zuo, J. Nan, L. Wang, Appl. Catal. B: Environ. 148–149 (2014) 154–163.
[28] X. Xiao, R. Hao, X. Zuo, J. Nan, L. Li, W. Zhang, Chem. Eng. J. 209 (2012) 293–300.
[29] K.G. Keramidas, G.P. Voutsas, P.I. Rentzeperis, Z. Kristalogr. 205 (1993) 35–40.
[30] K.L. Zhang, C.M. Liu, F.Q. Huang, C. Zheng, W.D. Wang, Appl. Catal. B: Environ. 68 (2006) 125–129.
[31] J. Cao, B.Y. Xu, B.D. Luo, H.L. Lin, S.F. Chen, Catal. Commun. 13 (2011) 63–68.
[32] J. Zhang, F. Shi, J. Lin, D. Chen, J. Gao, Z. Huang, X. Ding, C. Tang, Chem. Mater. 20 (2008) 2937–2941.
[33] F. Dong, Y. Sun, M. Fu, Z. Wu, S.C. Lee, J. Hazard. Mater. 219–220 (2012) 26–34.
[34] C. Nasr, K. Vinodgopal, L. Fisher, S. Hotchandani, A.K. Chattopadhyay, P.V. Kamat, J. Phys. Chem. 100 (1996) 8436–8442.
[35] X.P. Lin, T. Huang, F.Q. Huang, W.D. Wang, J.L. Shi, J. Phys. Chem. B 110 (2006) 24629–24634.
[36] N.M. Dimitrijevic, B.K. Vijayan, O.G. Poluektov, T. Rajh, K.A. Gray, H. He, P. Zapol, J. Am. Chem. Soc. 133 (2011) 3964–3971.
[37] W. He, H.K. Kim, W.G. Wamer, D. Melka, J.H. Callahan, J.J. Yin, J. Am. Chem. Soc. 136 (2014) 750–757.
[38] S. Shenawi-Khalil, V. Uvarov, S. Fronton, I. Popov, Y. Sasson, Appl. Catal. B: Environ. 117–118 (2012) 148–155.
[39] W. He, H. Jia, W.G. Wamer, Z. Zheng, P. Li, J.H. Callahan, J.J. Yin, J. Catal. 320 (2014) 97–105.
[40] H. Fu, C. Pan, W. Yao, Y. Zhu, J. Phys. Chem. B 109 (2005) 22432–22439.
[41] S. Kim, W. Choi, Kinetics, Environ. Sci. Technol. 36 (2002) 2019–2025.
[42] X. Zhu, J. Zhang, F. Chen, Appl. Catal. B: Environ. 102 (2011) 316–322.
[43] M.C. Yin, Z.S. Li, J.H. Kou, Z.G. Zou, Environ. Sci. Technol. 43 (2009) 8361–8366.
[44] L.S. Zhang, K.H. Wong, H.Y. Yip, C. Hu, J.C. Yu, C.Y. Chan, P.K. Wong, Environ. Sci. Technol. 44 (2010) 1392–1398.
[45] S.G. Meng, D.Z. Li, M. Sun, W.J. Li, J.X. Wang, J. Chen, X.Z. Fu, G.C. Xiao, Catal. Commun. 12 (2011) 972–975.
[46] G. Li, K.H. Wong, X. Zhang, C. Hu, J.C. Yu, R.C.Y. Chan, P.K. Wong, Chemosphere 76 (2009) 1185–1191.